



## CFD method for the liquid–gas two-phase flow fields in an Orbal oxidation ditch

Wenli Wei\*, X. Chen, W.L. Lou, Y. Cai, J. Wei, Y. Zheng

State Key Laboratory of Eco-hydraulics in Northwest Arid Region of China, Xi'an University of Technology, Xi'an, Shaanxi 710048, China, Tel. +86 15596886263; email: wei\_wenli@126.com (W. Wei), Tel. +86 15594170762; email: 1435999099@qq.com (X. Chen), Tel. +86 13227818087; email: 1052568599@qq.com (W.L. Lou), Tel. +86 15191913820; email: Yxicai@126.com (Y. Cai), Tel. +86 18629352022; email: Jwei1995@126.com (J. Wei), Tel. +86 13991987708; email: Zhengyan@126.com (Y. Zheng)

Received 15 January 2018; Accepted 29 July 2018

---

### ABSTRACT

This paper is concerned with a numerical simulation method for the flow fields in an Orbal oxidation ditch (OD). The velocity and pressure fields are obtained by solving the three-dimensional time-averaged Navier–Stokes equations and renormalized group  $k$ – $\epsilon$  turbulence model using Fluent 6.3.26. Combined with the multi-reference frame, the flow driven by a surface aerator was calculated. The finite volume method was used to discretize the differential equations; velocity and pressure were computed with the pressure-implicit with splitting of operators algorithm; and the simulation of free surface was carried out using the volume of fluid method. The numerical simulation was carried out according to the working conditions of the Orbal OD, and the simulated longitudinal velocities at the measuring points along the representative measuring lines were obtained. The comparison between the simulated longitudinal velocities and the experimental ones shows a better agreement, which essentially validates the reliability of the mathematical model. At last, the possible sources of various errors in the calculation and experiment are analyzed so as to beneficially improve the calculation and the measurement accuracy in the future.

*Keywords:* CFD; Flow fields; Orbal OD; Multi-reference frame; Experiment

---

### 1. Introduction

Oxidation ditch (OD) has the advantages of simple process, stable operation, and high removal rate of chemical oxygen demand (COD), and has been widely used in small and medium sewage treatment plants all over the world [1–5]. At present, there are 9,200 wastewater treatment plants in the United States using OD process, and only about more than 40 ODs in China [6]. The flow field characteristics of the OD determine the mixing degree of liquid in the ditches and the distribution of dissolved oxygen (DO) [7]. The operation practice shows that the flow region with low velocity in the ditch can cause the decrease of mixed fluidity, sludge deposition, the poor treatment effect, and the increase

of energy consumption [8,9]; therefore, it is of significance to study the flow fields in ODs. Tiranuntakula et al. [10] studied the integrated OD technology with biofilm reactor and the treatment capacity of the new OD from the aspects of DO, biochemical oxygen demand, and COD. Argaman and Spivak [11] proposed a prediction formula of average velocity for OD by using the principle of momentum conservation, by which the practical measurement results of circulation liquid in the ditch was analyzed. Simon et al. [12] developed a theoretical model based on mass and momentum balance to predict the average circulation speed of fluid generated by impellers, and the comparison between the experimental and simulation results coincides well. Li [13] used the experimental and simulation methods to study the flow fields of oval and round Orbal ODs, by which the rationality of equipment

---

\* Corresponding author.

configuration was analyzed, and the measures for improving the velocity distribution was put forward. Yang et al. [14] used computational fluid dynamics (CFD) software to simulate the flow fields and the distribution of DO in an OD. The influence of the position of surface aerator and the submerged depth of impeller on the distribution of DO and the flow pattern in the reactor were also discussed. Fan et al. [15] used CFD to simulate the three-dimensional (3D) flow fields and water dynamic characteristics of OD with surface aerator like an inverted umbrella, and also calculated the velocity of liquid phase and the volume fraction of solid phase. The simulation results are in good agreement with the test ones obtained by particle dynamic analyzer, which shows that the vertical velocity of solid phase is slightly lower than that of liquid phase, and the increasing of flow velocity in the reactor resulted in an increase in the liquid phase velocity, and the distribution of solid phase be more uniform. Wei et al. [16] simulated the effect of guiding baffles downstream from surface aerators on the flow fields in an OD using the CFD method. The comparison of the velocity distributions between the two conditions (with and without guiding baffles) shows that the installed guiding baffles downstream from the surface aerators can increase the velocity at the ditch bottom, and the vertical velocity distributions in the OD become more uniform. Wei et al. [17] used an experimentally validated numerical tool to study the effect of the submergence depth of impellers on flow fields in an OD and obtained an optimal submergence depth ratio of 0.45, which can better improve the efficiency of ODs in wastewater treatment system. Karpinska and Bridgeman [18] accounted for the actual flow field and its impact on the oxygen mass transfer and yield of the biological processes occurring in the aeration tanks. Xie et al. [19] proposed a two-phase (liquid–solid) CFD model to simulate the flow field and sludge settling in a full-scale Carrousel OD, by which an optimized operation scheme of the OD was obtained. Compared with the existing one, the volume fraction of solid phase at the bottom of the OD in the optimized operation scheme decreases from 0.260 to 0.258, and the distribution of sludge becomes uniform. Guo et al. [20] monitored and simulated the flow velocity and DO concentration in the outer channel of an Orbal OD system in a wastewater treatment plant in Beijing (China) under actual operation conditions, which shows that the flow velocity was heterogeneous in the outer channel, making the DO also heterogeneously distributed in the outer channel and the concentration gradients occur along the flow direction as well as in the cross section. The above researches [1–20] mainly study the hydraulic characteristics and the structural optimization of Carrousel ODs by means of experimental or numerical simulation methods. The experimental measurements mainly focus on the single-phase fluid (water) characteristics, not containing the motion characteristics of gas phase. The numerical simulations mostly use a single-phase flow model to simulate the characteristics of single-phase fluid (water) flow. Nevertheless, these explorations laid the foundation for studying the liquid–gas two-phase flow fields in an OD.

Based on the above references [1–20], the purpose of this paper is to use CFD method to study liquid–gas two-phase flow fields in an Orbal OD. The numerical simulation was carried out according to the working conditions of the Orbal OD, by which the simulated longitudinal velocities at the

measuring points along the representative measuring lines were obtained, and then were compared with the experimental ones to validate the reliability of the mathematical model. Finally, the possible sources of various errors in the calculation and experiment are also discussed and analyzed so as to beneficially improve the calculation and the measurement accuracy in the future.

## 2. Mathematical model

### 2.1. Governing equations

The unsteady incompressible time-averaged mass and momentum conservation equations can respectively be written as follows [16,17]:

$$\frac{\partial \rho}{\partial t} + \frac{\partial(\rho u_i)}{\partial x_i} = 0 \quad (1)$$

and

$$\frac{\partial(\rho u_i)}{\partial t} + \frac{\partial(\rho u_i u_j)}{\partial x_j} = -\frac{\partial p}{\partial x_i} + \frac{\partial}{\partial x_j} \left[ \mu \left( \frac{\partial u_i}{\partial x_j} + \frac{\partial u_j}{\partial x_i} \right) \right] - \frac{\partial}{\partial x_j} (\overline{\rho u_i' u_j'}) + \rho g_i \quad (2)$$

where  $\rho$  is density;  $t$  is time;  $x_i$  is the space coordinate in  $i$ -direction;  $p$  is pressure;  $\mu$  is molecular kinematic viscosity;  $g_i$  is the gravitational acceleration in  $i$ -direction;  $u_i$  and  $u_i'$  are the time-averaged and the fluctuating velocity components in  $i$ -direction, respectively; and the subscripts  $i, j = 1, 2, 3$ .

The term,  $-\overline{\rho u_i' u_j'}$ , defined as Reynolds stress in Eq. (2), must be modeled. In all the two-equation turbulence models, the modeling approach of Reynolds stress always employs the Boussinesq hypothesis taking the turbulence as locally isotropic turbulence; therefore, the formula for the Reynolds stress can be written as follows [17]:

$$-\overline{\rho u_i' u_j'} = \mu_t \left( \frac{\partial u_i}{\partial x_j} + \frac{\partial u_j}{\partial x_i} \right) - \frac{2}{3} \left( \rho k + \mu_t \frac{\partial u_i}{\partial x_i} \right) \delta_{ij} \quad (3)$$

where  $\mu_t$  is the turbulent viscosity, and computed as a function of turbulent kinetic energy,  $k$ , and kinetic energy dissipation rate,  $\varepsilon$  [16,17]:

$$\mu_t = \rho C_\mu \frac{k^2}{\varepsilon} \quad (4)$$

where  $C_\mu$  is a model constant with a value of 0.085.

The transport equations for  $k$  and  $\varepsilon$  in the renormalized group  $k$ - $\varepsilon$  turbulence model are given as follows [16,17]:

$$\frac{\partial(\rho k)}{\partial t} + \frac{\partial(\rho k u_i)}{\partial x_i} = \frac{\partial}{\partial x_j} \left[ \left( \mu + \frac{\mu_t}{\sigma_k} \right) \frac{\partial k}{\partial x_j} \right] + G_k - \rho \varepsilon \quad (5)$$

and

$$\frac{\partial(\rho\varepsilon)}{\partial t} + \frac{\partial(\rho\varepsilon u_i)}{\partial x_i} = \frac{\partial}{\partial x_j} \left[ \left( \mu + \frac{\mu_t}{\sigma_\varepsilon} \right) \frac{\partial \varepsilon}{\partial x_j} \right] + C_1 \frac{\varepsilon}{k} G_k - \rho C_2 \frac{\varepsilon^2}{k} \quad (6)$$

where  $\sigma_k$ ,  $C_2$ , and  $\sigma_\varepsilon$  are empirical constants and have the values of 0.7179, 1.68, and 0.7179, respectively; and other parameters are as follows:  $C_1 = 1.42 - \eta(1 - \eta/\eta_0)/(1 + \beta\eta^3)$ ,  $\eta_0 = 4.38$ ,  $\beta = 0.015$ ,  $\eta = Sk/\varepsilon$ ,  $S = (2S_{ij}S_{ij})^{1/2}$ , and  $S_{ij} = (\partial u_i/\partial x_j + \partial u_j/\partial x_i)/2$ .

### 2.2. Simulation of water-free surface

Volume of fluid (VOF) method was used to simulate the water-free surface. The basic idea of the VOF method [16,17] is to determine and track the change of fluid surface according to the ratio function,  $F_w(t, x_i)$ , of the fluid volume within a cell to the cell volume. For a calculation cell,  $F_w(t, x_i) = 0$  means that there is no liquid in the cell;  $F_w(t, x_i) = 1$  means that the cell is fully filled with liquid; and  $0 < F_w(t, x_i) < 1$  means that the cell is partially filled with liquid.

The interface between liquid and air is tracked by solving the equation of  $F_w(t, x_i)$ , which is written as follows [16,17]:

$$\frac{\partial F_w}{\partial t} + \frac{\partial(F_w u_i)}{\partial x_i} = 0 \quad (7)$$

where  $t$  is time;  $u_i$  and  $x_i$  ( $i = 1, 2, 3$ ) are the velocity and coordinate components in  $i$ -direction, respectively.

After the use of VOF,  $\rho$  and  $\mu$  are a function of  $F_w(t, x_i)$ , and can be expressed as follows [16,17,21]:

$$\rho = (1 - F)\rho_a + F\rho_w \quad (8)$$

$$\mu = (1 - F)\mu_a + F\mu_w \quad (9)$$

where  $\rho_a$  and  $\mu_a$  are the density and viscosity of air, respectively; and  $\rho_w$  and  $\mu_w$  are the density and viscosity of water, respectively.

### 3. Experimental model and measurement method

The physical OD model with measured data from the study by Wei et al. [22] is used to validate the mathematical model. The OD model consists of two rectangular channels, two curved channels, and a surface aerator. The rectangular channel has a length of 243 cm; the radii of the walls of curved channels are 93.5 and 63.5 cm, respectively; and the channels have a width of 30 cm. The size of the model is shown in Fig. 1. The effective water depth in the OD is 22 cm, and the draft depth of the aerator is 6.3 cm. The surface aerator is composed of 12 discs, and is installed at 45 cm downstream of the link between the curved and straight channels. The shape of the surface aerator is shown in Fig. 2. Figs. 2(a) and (b) show the 3D geometry and the meshes for the surface aerator. The detail dimensions of the surface aerator are shown in Fig. 3. Fig. 3(a) shows that the length of the surface aerator is 0.22 m and that the distance between the nearby blades is 0.02 m, and Fig. 3(b) shows that the diameter of the surface aerator is 0.15 m.

The experiment was carried out by using an acoustic Doppler velocimeter made by the American company SonTek, San Diego, CA. The instrument can directly measure the instantaneous 3D velocities and turbulence parameters with a high measurement precision and also has smaller disturbance to the flow. It has easy operation and strong processing power. The three measurement sections downstream from the aerator is shown in Fig. 1(b), in which three vertical lines numbered as 1, 2, and 3, from the outside to inside of the OD, are arranged (in Fig. 4) for the analysis of velocity distribution. Along the three vertical lines, each distance between two nearby measuring points is about 1 cm.

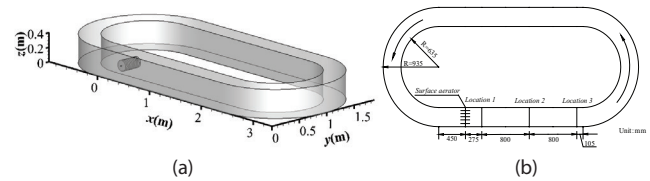


Fig. 1. Schematic diagram of the Orbal OD: (a) 3D computational domain and (b) detail dimensions of the Orbal OD.

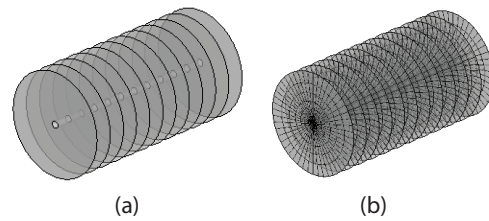


Fig. 2. Geometry of the surface aerator: (a) 3D geometry and (b) grids for the 3D geometry.

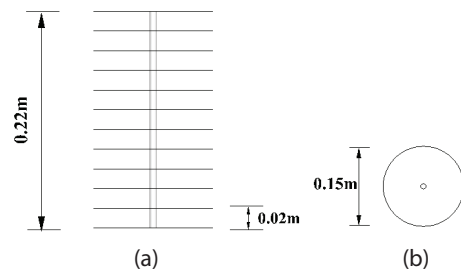


Fig. 3. Detail dimensions of the surface aerator: (a) view from the top and (b) view from the side.

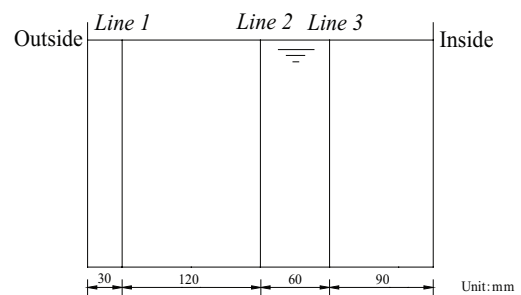


Fig. 4. Vertical measuring lines in sections.

**4. Computational region and grid generation**

The grid of the computational region uses a structured one. Compared with the size of the whole computational region, the thickness of the aerator is much small; therefore, the aeration disk is taken as an infinite thin one, and the mesh near the aerator is refined for the improvement of the grid quality. The total grid number is 210,600. The 3D grid of the 3D region is shown in Fig. 5(a), and the two-dimensional grid from top view is shown in Fig. 5(b). The computational mesh independence was discussed in Section 7.3.

**5. Initial conditions and boundary conditions**

The initial water depth is 0.22 m, and velocity is zero. The relative pressure value, 0, is given as the boundary condition for the top surface of the calculation model, and the wall function is taken as the boundary condition at the solid walls. The multi-reference frame model is adopted to simulate the aerator with a rotational speed of 198 rpm. The free water surface is captured by the VOF method. The time step is 0.005 s. The process of numerical calculation is achieved by an iterative method. Therefore, the calculation convergence criterion is that the absolute value of the maximum difference between the calculated values of the two adjacent iterations for the physical quantities is less than  $10^{-4}$ .

**6. Analysis of results**

*6.1. Analysis of the simulated gas–liquid surface*

The simulated gas–liquid surface (water surface) in the OD is shown Fig. 6, from which it can be seen that the water surface in the straight channels is almost a plane, while in the bend channels is a curved surface; the water surface is higher outside than inner side of the bends. This phenomenon is mainly caused by the centrifugal force acting on the fluid when the flow passes through the bends. Besides, the rotation

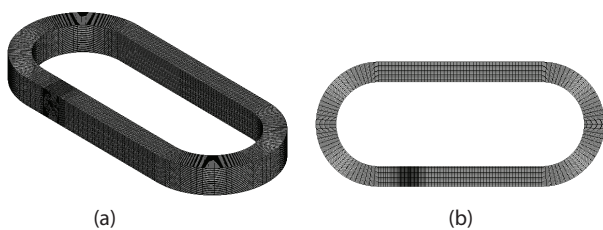


Fig. 5. Grid of computational domain: (a) 3D grid and (b) 2D grid from top view.

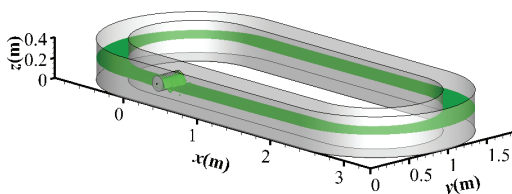


Fig. 6. 3D diagram of the simulated gas–liquid surface (water surface) in the OD.

of the surface aerator takes some water with it because of the viscosity of water.

*6.2. Analysis of the simulated velocity, streamline, and turbulent kinetic energy in the three horizontal planes*

The simulated velocity and streamline charts in the three horizontal planes, respectively, through the vertical coordinate points  $z = 0.14$  m,  $z = 0.11$  m, and  $z = 0.02$  m, are shown in Fig. 7, and the simulated turbulent kinetic energy is shown in Fig. 8. It can be seen from Fig. 7 that the velocity in the horizontal plane close to the surface aerator is maximum, in the middle plane the second, and near the ditch bottom the smallest, and the distributions of the turbulent kinetic energy in the three horizontal planes have the same law, that is, the upper is maximum, the middle the second, and the lower the smallest. The cause of flow motion is that the rotation of the surface aerator makes the water contacting it to move by the viscosity of water, and the driven water makes the near water to move so that the total water under the surface aerator moves. This velocity distribution can be explained from the angle of water energy loss, in vertical direction, the farther the point to the surface aerator is, the smaller is the flow velocity at the point. The change of turbulence kinetic energy in Fig. 8 corresponds to that of velocity in Fig. 7; the bigger the velocity is, the bigger is the corresponding turbulence kinetic energy.

*6.3. Analysis of the velocity distribution along vertical lines*

The experimental values along the representative measuring lines in the three cross sections (in Fig. 1(b)) under the working condition were compared with the numerically simulated velocities to validate this mathematical model. The three representative cross sections with vertical lines numbered from outer to inner side as Line 1–Line 3 are selected (in Fig. 4).

Fig. 9 shows the comparisons of velocity distributions along the three vertical lines in the three cross sections between the experimental values and simulated ones, in which the transverse coordinate shows the relative

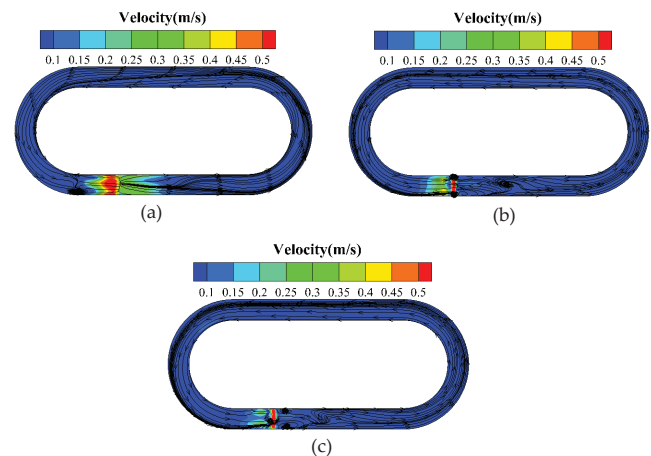


Fig. 7. Simulated velocity and streamline in the three horizontal planes: (a)  $z = 0.14$ , (b)  $z = 0.11$  m, and (c)  $z = 0.02$  m.

velocity,  $u/v$ , where  $u$  is the longitudinal velocity (in flowing direction) at a point along a vertical measuring line,  $v$  is the depth-averaged velocity along the vertical measuring line, and computed by  $(v = \frac{1}{H} \int_0^H u dz)$ , where  $H$  is the total water depth of the OD; and the longitudinal coordinate shows the relative vertical distance,  $z/H$ , where  $z$  is the distance from

the point to the ditch bottom in vertical direction, and  $H$  is the water depth.

The comparisons between the simulated longitudinal velocities and the experimental ones are in good agreement. But in the area near the water surface, especially closer to the aerator in Cross section 1, the simulated velocity values have a slight difference with the measured ones, the reason of which is that the rotating aerator makes its nearby fluid run much faster as if the upper part of the coming uniform flow was made like a turbulent jet in a straight channel downstream of the rotating aerator, and the turbulent jet forms a much mixed turbulent flow resulting in a difference between the simulated longitudinal velocities and the experimental ones near the water surface. In addition, for the improvement of the computational grid quality, the aeration disk is taken as an infinite thin one diffident from the actual aeration disk, which may also result in a certain error in the calculation.

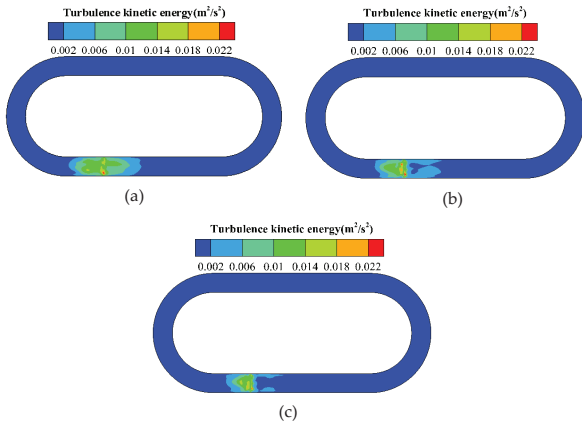


Fig. 8. Simulation turbulent kinetic energy in the three horizontal planes: (a)  $z = 0.14$ , (b)  $z = 0.11$  m, and (c)  $z = 0.02$  m.

6.4. Analysis of the velocity distributions along horizontal lines

Fig. 10 shows the comparisons of the simulated longitudinal velocity distributions with the experimental ones along each measuring line in the three cross sections of Location 1–Location 3, in which the horizontal coordinate shows the relative distance,  $l/B$ , where  $l$  is the distance from a measuring point to the outside wall of the ditch, and  $B$  is the width of the ditch; and the longitudinal coordinate shows the relative velocity,  $u/v$ , where  $u$  is the longitudinal velocity (in flowing direction) at a point corresponding to horizontal line,  $z/H$ , and vertical line,  $l/B$ , in a cross section, and  $v$  is the depth-averaged velocity along a vertical measuring line,  $l/B$ , of the cross section. The three relative heights of  $z/H$  along the vertical measuring lines in the three cross sections are 0.25, 0.50, and 0.75, respectively, where  $z$  is the distance from the point to ditch bottom, and  $H$  is the total water depth.

The comparisons between the simulated longitudinal velocities and the experimental ones show a good agreement. With the mixed turbulent jet flow, the velocity difference along the horizontal measuring lines,  $z/H$ , in Cross section 1 is larger, especially at the outer side (side with smaller  $l/B$ ) and the inner side (side with larger  $l/B$ ); besides, the distributions of velocity is much non-uniform owing to Cross section 1 being nearer to the bend outflow. Compared with Cross section 1, the velocity distribution along  $z/H$  horizontal measuring lines in Cross section 2 is more relatively uniform, and in Cross section 3 much more uniform, which results from cross sections 2 and 3 being farther and farther away from the bend outflow and the straight open channel making flows become more and more uniform. It is also seen that the velocity distributions along the  $z/H$  horizontal measuring lines in the three cross sections are obviously non-uniform in vertical direction, and the most non-uniform appears at  $z/H = 0.75$  (near water surface), while the most uniform at  $z/H = 0.25$  (near ditch bottom).

In addition, Cross section 1 is nearest to the bend and the aeration disk, so the upstream coming flow mostly influences the distribution of velocity in Cross section 1, and its influence on cross sections 2 and 3 gradually weakens; therefore, the velocity difference between the inside and outside of cross sections 2 and 3 is small.

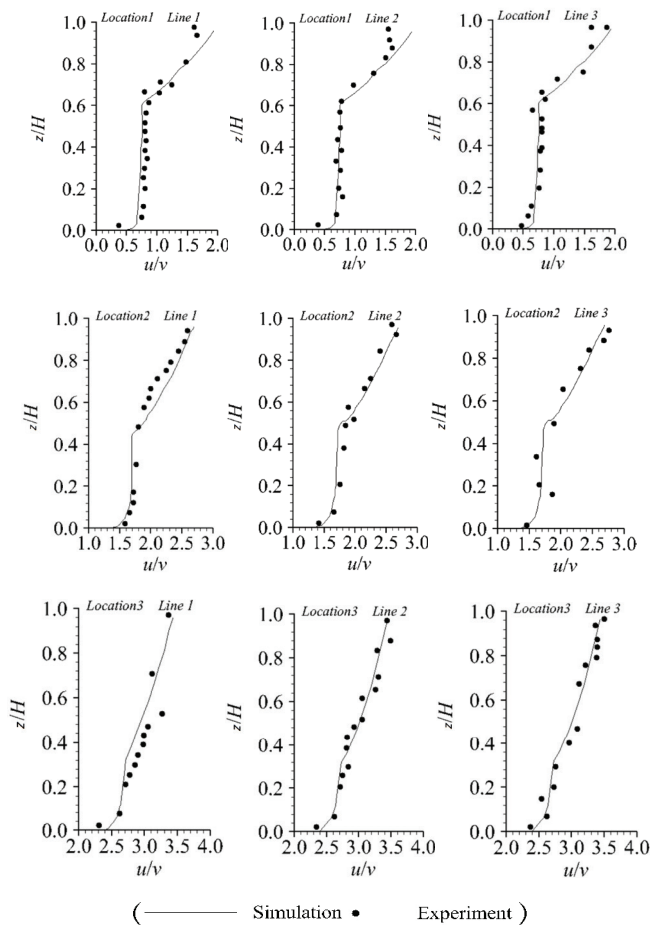


Fig. 9. Comparisons of longitudinal velocities between the simulated and experimental ones along vertical measuring lines.

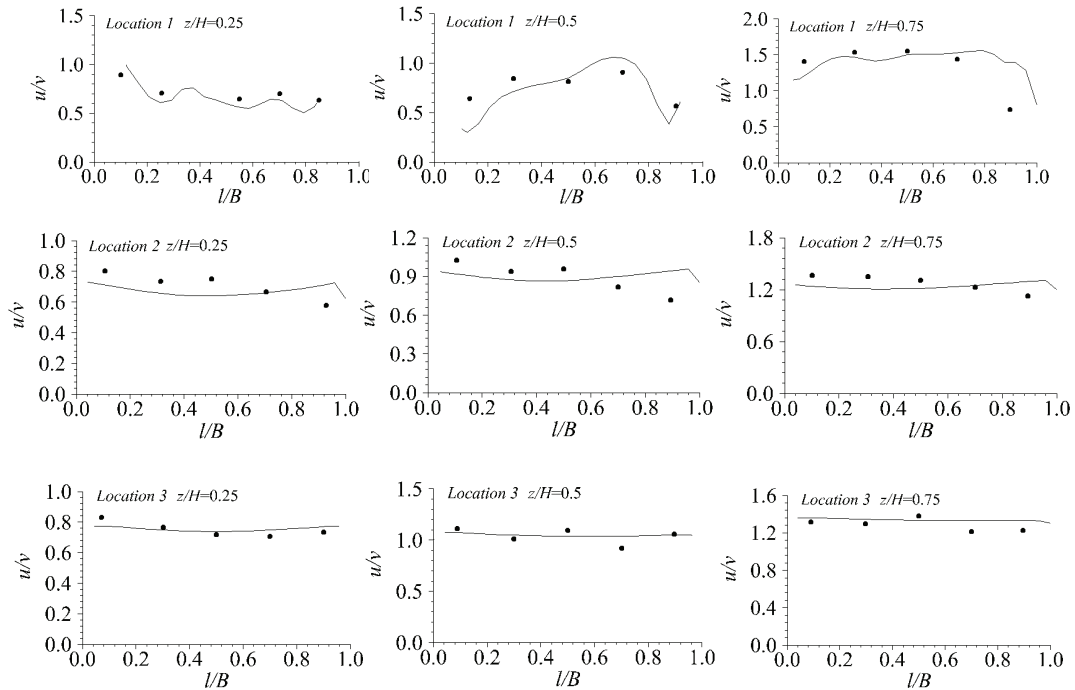


Fig. 10. Comparisons of the longitudinal velocity between the simulated and experimental ones along  $z/H$  measuring lines.

## 7. Discussions

### 7.1. Qualitative analysis of possible sources of various errors

The possible sources of various errors in the calculation and experiment are analyzed as follows so as to beneficially improve the calculation and measurement accuracy in the future.

Mathematical models produce errors. Whether the selected mathematical model can well describe the problem or not is a key factor. In this paper, the proposed mathematical model can well describe streamline bend flows; therefore, it can well solve the flow fields in an Orbal OD. Sometimes, physical models are often simplified locally in calculation so as to improve the grid quality, but this may produce errors. In this calculation, compared with the size of the whole computed area, the thickness of the aerator is much small; therefore, the simulated aeration disk is taken as an infinite thin one, but this may produce errors.

Numerical errors are often divided into two kinds, such as truncation error and rounding error. If the boundary condition is not a Dirichlet case, then the boundary condition is discretized in the solution to differential equations, so an additional truncation error (boundary truncation error) is introduced. From this point, the order of the total discrete error should be of the lowest order of the truncation error. In the solution method of differential equations, especially for iterative solution method, rounding error is also introduced, which is due to the restriction of the counting length of the computer. The influence of space and time steps on the discrete truncation error is contrary to that on rounding errors. The discrete truncation error decreases as the step size decreases, while rounding error generally increases with step size. Therefore, we should draw a conclusion that reducing the step size will improve the computational accuracy.

### 7.2. MAE analysis of specific data of errors between the simulated velocities and experimental ones

In statistics, the mean absolute error (MAE) is a quantity used to measure how close forecasts or predictions are to the eventual outcomes. The MAE is an average of the absolute errors, and given by

$$\text{MAE} = \frac{1}{N} \sum_{i=1}^N |e_i| \quad (10)$$

where  $e_i = |f_i - y_i|$  is an absolute error,  $f_i$  is a simulated value, and  $y_i$  is an experimental one.

According to Eq. (10), the MAE for each line in the three cross sections can be computed, as shown in Table 1. It is known from Table 1 that the computed MAE for Line 1 in the three cross sections is bigger than that of other two lines, which shows that the simulated velocities ( $u/v$ ) and experimental ones for Line 1 in the three cross sections have a poor agreement, while for Lines 2 and 3 a better agreement. The analysis results are consistent with the display of Fig. 9.

The specific data of errors between the simulated velocities ( $u/v$ ) and experimental ones for each vertical line in the three cross sections are shown in Table 2, from which it is known that, in Cross section 1, the relative maximum error percentage is 10.43% at a point in Line 1; in Cross section 2, 14.58% at a point in Line 1; and in Cross section 3, 8.11% also at a point in Line 1. This appearance corresponds to the case of Table 1, showing that the specific data of errors between the simulated velocities and experimental ones have a serious influence on the value of MAE. Totally speaking, the simulated velocities and experimental ones at the most of measuring points in the three cross sections have a good agreement,

Table 1  
Mean absolute error (MAE) of velocities ( $u/v$ ) for each line in the three cross sections

Number of cross sections	Location 1			Location 2			Location 3		
	Line 1	Line 2	Line 3	Line 1	Line 2	Line 3	Line 1	Line 2	Line 3
Computed MAE for each line	0.0963	0.0838	0.0894	0.0991	0.0752	0.0885	0.1209	0.0674	0.0691

Table 2  
Specific data of errors between the simulated velocities ( $u/v$ ) and experimental velocities along each line in the three cross sections

Number of cross section	Location 1			Location 2			Location 3		
	Line 1	Line 2	Line 3	Line 1	Line 2	Line 3	Line 1	Line 2	Line 3
Specific datum of maximum errors	0.2124	0.1239	0.1947	0.2727	0.2727	0.1818	0.2637	0.1319	0.1319
Relative maximum error percentage (%)	10.13	4.78	10.43	14.58	14.39	13.79	8.11	3.77	4.26
Specific datum of minimum errors	0.0177	0.0177	0.0177	0.0454	0.0227	0.0454	0.0220	0.0220	0.0220
Relative minimum error percentage (%)	0.99	0.66	1.21	3.03	2.85	5.26	0.81	0.81	0.84

but at a few points have a bigger difference; therefore, at the points with a bigger difference the experimental values may have a mistake.

### 7.3. Quantitative analysis of simulations with different grid densities

The simulations with different grid densities named as Grid 1, Grid 2, Grid 3, and Grid 4 have been performed. The grids 1, 2, 3, and 4 have 177,846, 197,632, 210,600, and 231,606 meshes, respectively, among which the computational mesh independence has been done to meet the requirement of the numerical simulation. Under the same initial and boundary conditions, the flow fields for the OD of grids 1, 2, 3, and 4 are, respectively, simulated, and the velocity components in  $x$ -direction along the vertical line at a point 120 mm downstream from Cross section 3 are displayed in Fig. 11, which shows that the simulated results of grids 3 and 4 are nearly the same, and greater than those of grids 1 and 2. The good agreement between grids 3 and 4 validates that the Grid 3 with 210,600 meshes is an independent one.

### 7.4. Comparison of the typical Reynolds numbers between the model and its prototype

The dimensions of the model are much smaller than the full-scale OD, so it is essential to compare the typical Reynolds number from the industrial reactor with the one in this work.

In the OD model, the OD model has a width of 30 cm, the effective water depth is 22 cm in the straight channel, and the average velocity over Cross section 3 is 0.03589 m/s; while in the OD prototype, the OD has a width of 7.5 m, the effective water depth is 5.5 m in the straight channel, and the average velocity over Cross section 3 is 0.17945 m/s. The hydraulic radius is defined as  $R_h = A/P$ , where  $A$  is the cross-sectional area of the flowing fluid, and  $P$  is the wetted perimeter, that the portion of the perimeter of the cross section where the fluid contacts the solid boundary, and therefore where friction

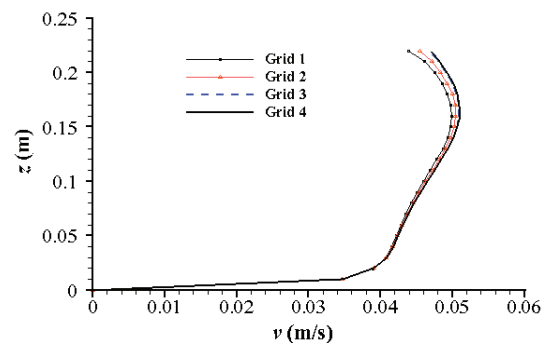


Fig. 11. Comparisons of the velocity components in  $x$ -direction along a vertical line for the four kinds of grid.

resistance is exerted on the flowing fluid. The Reynolds number is defined as  $Re = vR_h/\nu$ , where  $\nu = 1.792 \times 10^{-6} \text{ m}^2 \text{ s}^{-1}$  is the water kinematic viscosity. According to this formula for computing Reynolds number, the typical Reynolds numbers from the industrial reactor and the one in this work over Cross section 3 of the channel are 223,281 and 1,786.3, respectively, from which it is known that the flows in the model and its prototype are both turbulent because of their typical Reynolds numbers being both greater than 500 [23].

## 8. Conclusions

The numerical simulation was carried out according to the working conditions of an Orbal OD, and the simulated longitudinal velocities at measuring points along representative measuring lines were obtained. The simulated longitudinal velocities are in good agreement with the experimental ones, which validates that the mathematical model and the solution method can well solve the flow fields in an Orbal OD. Therefore, the mathematical model can provide an effective method in studying the hydraulics of Orbal ODs.

In the three cross sections, the maximum relative error percentage, 14.58%, between the simulated velocities and

experimental ones corresponds to the value of MAE, which shows that the specific data of errors between the simulated velocities and experimental ones have a serious influence on the value of MAE. In addition, the possible sources of various errors in the calculation and experiment are analyzed so as to beneficially improve the calculation and the measurement accuracy in the future.

In further study, based on the research work, gas–liquid–solid flow fields will be studied in the numerical simulation of Orbal ODs.

## Acknowledgments

Financial support of this study was from the National Natural Science Foundation of China (Grant No. 51578452 and No. 51178391) and the scientific research projects of Shaanxi Province (2016GY-180, 2014K15-03-05). In addition, the authors would like to thank the researchers performing the experimental work.

## Symbols

$B$	—	Width of the straight channel in OD, m
$C_\mu$	—	Model parameter in Eq. (4) with a value of 0.085
$C_1$	—	Model parameter in Eq. (6)
$C_2$	—	Model parameter in Eq. (6) with a value of 1.68
$F_w$	—	The ratio of fluid volume within a cell to the cell volume
$g_i$	—	Gravitational acceleration in $i$ -direction, $i = 1, 2, 3$ , m/s <sup>2</sup>
$H$	—	The water depth, m
$k$	—	Turbulent kinetic energy, m <sup>2</sup> /s <sup>2</sup>
$p$	—	Pressure, kg/m <sup>3</sup> s <sup>2</sup>
$G_k$	—	Production term in Eqs. (5) and (6)
$R$	—	Radius of bends, m
$S$	—	Parameter for computing $C_1$
$S_{i,j}$	—	Parameter for computing $C_1$
$t$	—	Time, s
$u_i$	—	Velocity component in $i$ -direction, $i = 1, 2, 3$ , m/s
$u'_i$	—	Fluctuating velocity component in $i$ -direction, $i = 1, 2, 3$ , m/s
$x_i$	—	Space coordinate in $i$ -direction, $i = 1, 2, 3$ , m
3D	—	Three-dimensional
COD	—	Chemical oxygen demand
CFD	—	Computational fluid dynamics
DO	—	Dissolved oxygen
OD	—	Oxidation ditch
VOF	—	Volume of fluid

## Greeks

$\beta$	—	A constant of 0.015 for computing $C_1$
$\delta_{ij}$	—	Kronecker function in Eq. (3), $\delta_{ij} = 1$ with $i = j$ , and $\delta_{ij} = 0$ with $i \neq j$
$\varepsilon$	—	Kinetic energy dissipation rate, m <sup>2</sup> /s <sup>3</sup>
$\eta$	—	Parameter for computing $C_1$
$\eta_0$	—	Constant of 4.38 for computing $C_1$
$\mu$	—	Molecular kinematic viscosity, kg/(m <sup>3</sup> s)
$\mu_t$	—	Turbulent viscosity, kg/(m <sup>3</sup> s)

$\rho$	—	Density, kg/m <sup>3</sup>
$\sigma_k$	—	Model parameter in Eq. (5) with a value of 0.7197
$\sigma_\varepsilon$	—	Model parameter in Eq. (6) with a value of 0.7197

## Subscripts

$i, j$	—	Direction, $i = 1, 2$ , and $3$ ; $j = 1, 2$ , and $3$
$t$	—	Turbulence

## References

- [1] T. Hashimoto, K. Onda, Y. Nakamura, K. Tada, A. Miya, T. Murakami, Comparison of natural estrogen removal efficiency in the conventional activated sludge process and the oxidation ditch process, *Water Res.*, 41 (2007) 2117–2126.
- [2] K.J. Hartley, Controlling sludge settle ability in oxidation ditch process, *Water Res.*, 42 (2008) 1459–1466.
- [3] G. Liu, Y. Chong, Q. Fan, X. Jia, Sh. Li, Hydrodynamic effects of the oxidation ditch on the removal efficiency and energy consumption, *Environ. Sci.*, 27 (2006) 2323–2326 (in Chinese).
- [4] R. Deng, X. Zhang, T. Wang, H. Xiao, Technical and economic evaluation of oxidation ditch process, *Chin. Water Wastewater*, 23 (2007) 37–40 (in Chinese).
- [5] Y. Liu, H. Shi, Zh. Wang, G. Wang, X. Dai, Y. Wang, Variation of dissolved oxygen and optimum control conditions in Carrousel oxidation ditch, *Chin. Environ. Sci.*, 28 (2008) 843–846 (in Chinese).
- [6] Sh. Xia, J. Liu, An innovative integrated oxidation ditch with vertical circle for domestic wastewater treatment, *Process Biochem.*, 39 (2004) 1111–1117.
- [7] L. Luo, W. Li, R. Deng, Z. He, T. Wang, Simulation and analysis on three-dimensional flow field of integrative oxidation ditch, *Chin. Water Wastewater*, 19 (2003) 15–18 (in Chinese).
- [8] X. Zhao, Q. Zhang, T. Huang, P. Zhang, Sludge deposition analysis and hydraulic calculation of oxidation ditch bend, *Chin. Water Wastewater*, 24 (2008) 38–40 (in Chinese).
- [9] Zh. Chen, R. Yang, Numerical simulation of hydraulic characteristic of oxidation ditch with new corrugated plate guide wall, *Environ. Eng.*, 28 (2010) 33–35 (in Chinese).
- [10] M. Tiranuntakula, V. Jegatheesana, P.A. Schneider, H.L. Fracchia, Performance of an oxidation ditch retrofitted with a membrane bioreactor during the start-up, *Desalination*, 183 (2005) 417–424.
- [11] Y. Argaman, E. Spivak, Engineering aspects of wastewater treatment in aerated ring-shaped channels, *Water Res.*, 8 (1974) 317–322.
- [12] S. Simon, M. Roustan, J.M. Audic, P. Chatellier, Prediction of mean circulation velocity in oxidation ditch. *Environ. Tech.*, 22 (2001) 195–204.
- [13] Y. Li, AIRE-O2 Oxygenation Machine Performance Analysis and Orbal Oxidation Ditch Flow Test and 3D Simulation, PhD Thesis, Chongqing University, Chongqing, China, 2005.
- [14] Y. Yang, J. Yang, J. Zuo, Y. Li, Sh. He, X. Yang, K. Zhang, Study on two operating conditions of a full-scale oxidation ditch for optimization of energy consumption and effluent quality by using CFD model, *Water Res.*, 45 (2011) 3439–3452.
- [15] L. Fan, N. Xu, Zh. Wang, H. Shi, PDA experiments and CFD simulation of a lab-scale oxidation ditch with surface aerators, *Chem. Eng. Res. Des.*, 88 (2010) 23–33.
- [16] W. Wei, Z. Zhang, Y. Zheng, Y. Liu, Numerical simulation of additional guiding baffles to improve velocity distribution in an oxidation ditch, *Desal. Wat. Treat.*, 57 (2016) 24257–24266.
- [17] W. Wei, Y. Liu, B. Lv, Numerical simulation of optimal submergence depth of impellers in an oxidation ditch, *Desal. Wat. Treat.*, 57 (2016) 8228–8235.
- [18] A. M. Karpinska, J. Bridgeman, CFD-aided modelling of activated sludge systems—a critical review, *Water Res.*, 88 (2016) 861–879.

- [19] H. Xie, J. Yang, Y. Hu, H. Zhang, Y. Yang, K. Zhang, X. Zhu, Y. Li, Ch. Yang, Simulation of flow field and sludge settling in a full-scale oxidation ditch by using a two-phase flow CFD model, *Chem. Eng. Sci.*, 109 (2014) 296–305.
- [20] X. Guo, X. Zhou, Q. Chen, J. Liu, Flow field and dissolved oxygen distributions in the outer channel of the Orbal oxidation ditch by monitor and CFD simulation, *J. Environ. Sci.*, 25 (2013) 645–651.
- [21] S. Vedantam, J.B. Joshi, S.B. Koganti, Three-dimensional CFD simulation of stratified two-fluid Taylor-Couette flow, *Can. J. Chem. Eng.*, 84 (2006) 279–288.
- [22] Y. Wei, J. He, Zh. Li, Q. Liu, Hydraulic characteristics in straight section of oxidation ditch, *Environ. Sci. Technol.*, 35 (2012) 87–91.
- [23] E. John Finemore, Joseph B. Franzini, *Fluid Mechanics with Engineering Applications*, 10th ed., McGraw-Hill Companies, Inc., New York City, USA, 2002.